Supporting Information: Shape Changes in AuPd Alloy Nanoparticles Controlled by Anisotropic Surface Stress Relaxation

Diana Nelli,[†] Cesare Roncaglia,[†] Riccardo Ferrando,[*,‡,§] and Chloé Minnai[*,¶,§]

[†]*Dipartimento di Fisica dell'Università di Genova, via Dodecaneso 33, Genova 16146, Italy*

[‡]*Dipartimento di Fisica dell'Università di Genova and CNR-IMEM, via Dodecaneso 33, Genova 16146, Italy*

[¶]*Molecular Cryo-Electron Microscopy Unit, Okinawa Institute of Science and Technology Graduate University 1919-1 Tancha, Onna-son, Kunigami-gun Okinawa, Japan 904-0495*

[§]*Corresponding author*

E-mail: ferrando@fisica.unige.it; chloe.minnai@oist.jp

Experimental Methods

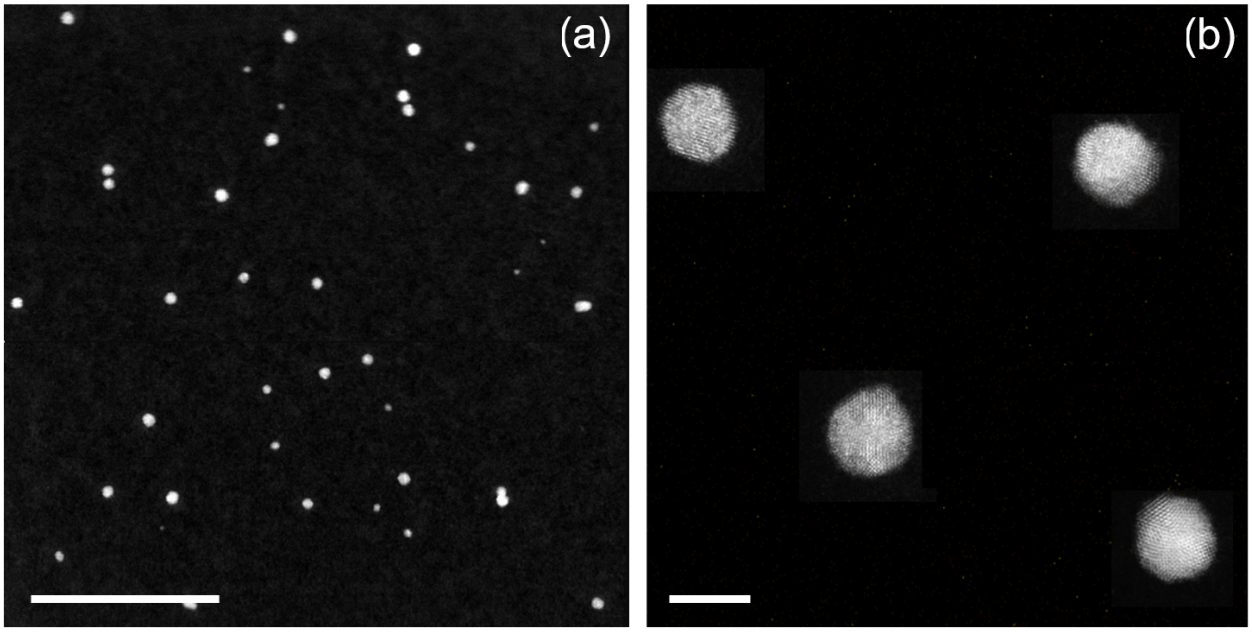

Figure S1: C_s-corrected STEM-HAADF image of $Au_{25}Pd_{75}$ NPs. (a) Low magnification image showing many nanoparticles. Scale bar 50 nm. (b) Larger magnification image showing the atomic structure of the nanoparticles. Scale bar 5 nm.

AuPd nanoparticles are synthesized by inert gas-aggregation sputtering deposition, using a Nanogen-Trio source (Mantis Deposition Ltd, UK). This technique is based on the condensation of an atomic vapor produced by DC simultaneous magnetron-sputtering of targets. As described in detail in Ref.,[1,2] the Nanogen-Trio source employs three separate circular 1″ targets mounted on the same linear translator within one region of inert gas aggregation, called aggregation zone. The sputtering current applied to the targets can be adjusted separately, thereby providing control over the mole fraction of metals incorporated into the nanoparticles. Here, two Au and Pd highly pure (99.99%) single metal targets are co-sputtered in an Ar flux of 70 sccm (standard cubic centimeters per minute) which originates in a Nanogen pressure of $2 \sim 10^{-1}$ mbar. The deposition chamber has a pressure of $P_{DC} = 10^{-4}$ mbar in standard operating conditions and can be further increased by flowing a controlled amount of Ar in the deposition chamber. The difference of pressure causes the nanoparticle extraction and acceleration from the aggregation zone to the deposition chamber where they soft land

onto substrates held at ground potential.

As deeply described in Ref.[3] the residence time in the aggregation zone (dwell time) can be increased both by rising the length of the aggregation zone (L_{AZ}) and by decreasing the pressure difference ΔP between the source and the deposition chamber (P_{DC}).

Here five growing conditions are tested: L_{AZ} = 45, 70, 95 and 125 mm with $P_{DC} = 6 \times 10^{-4}$ mbar and L_{AZ} = 125 mm with $P_{DC} = 4 \times 10^{-3}$ mbar.

The applied powers are varied to obtain pure Pd distributions and three Pd-rich compositions: $Au_{15}Pd_{85}$, $Au_{25}Pd_{75}$, $Au_{35}Pd_{65}$. These compositions are obtained setting respectively the following powers: P_{Pd}= 4.1 W; P_{Pd}= 9.2 W, P_{Au}= 4.5 W; P_{Pd}= 7.8 W, P_{Au}= 5.8 W; P_{Pd}= 4.1 W, P_{Au}= 5.9 W.

To obtain these recipes we first calculated the theoretically the powers to be applied to the targets to have the desired compositions of the atomic vapour. These are estimated by dividing the power applied to the target by the cohesion energy of the specific element ($E_{c,Pd}$=3.89 eV/atom and $E_{c,Au}$ =3.81 eV/atom).

However the effective composition of the nanoparticle distribution deposited on the substrate can be slightly different from the theoretical values. For this reason, at each composition several samples are fabricated and quantitatively characterised by performing EDX analysis of the composition. In this way it is possible to gradually adjust the powers applied to the targets so to obtain the desired compositions with an error inferior to 2%.

To unravel the features of the AuPd distribution, the nanoparticles are deposited directly on amorphous carbon coated TEM grids to yield random arrays of binary nanoparticles. The deposition time is varied so to have very low density of particles in the samples used for characterising the structure of the nanoparticles. In these samples the depositions last 180 seconds to avoid coalescence phenomena due to overlapping of the nanoparticles on the grid. The interparticle distances are at least 10 times their diameter. Larger densities of nanoparticles are deposited on the samples that are used for evaluating the composition of the AuPd distribution. In this case the depositions last at least 5 minutes; a result is shown

in Figure S1a.

The average composition, size and morphology of the nanoparticles are examined using an aberration-corrected scanning transmission electron microscopy (C_s-corrected-STEM), JEOL JEM-ARM 200F (this was operated at 200 kV to ensure a safe interaction with the nanoparticles). Scanning transmission electron microscopy combined with X-ray energy-dispersive spectroscopy (STEM–EDX) is also used to study elemental mapping for the respective elements.

Model and simulation methods

The atomistic potential has the form proposed by Gupta[4] and by Rosato *et al.*[5] This force field can be derived from the second moment approximation to the tight-binding model.[6] The potential energy E is the sum of one-atom contributions E_j containing a bonding (E_j^b) and a repulsive part (E_j^r):

$$E = \sum_j E_j = \sum_j (E_j^b + E_j^r), \tag{1}$$

where

$$E_j^b = -\sqrt{\sum_i \xi_{sw}^2 \exp\left[-2q_{sw}\left(\frac{r_{ij}}{r_{sw}^0} - 1\right)\right]}, \tag{2}$$

and

$$E_j^r = \sum_i A_{sw} \exp\left[-p_{sw}\left(\frac{r_{ij}}{r_{sw}^0} - 1\right)\right]. \tag{3}$$

r_{ij} is the distance between atoms i and j. s (w) refers to the chemical species of the atom i (j). If $s = w$, r_{sw}^0 is the nearest-neighbor distance in the corresponding bulk lattice, while for $s \neq w$, r_{sw}^0 is taken as the arithmetic mean of the distances of pure metals. Cutoff distances on the interactions are imposed as follows. The exponentials in Eqs. (2-3) are replaced by fifth-order polynomials, of the form $a_3(r-r_{c2})^3 + a_4(r-r_{c2})^4 + a_5(r-r_{c2})^5$, between distances r_{c1} and r_{c2}, with a_3, a_4, a_5 fitted in each case to obtain a function which is always continuous, with first and second derivative for all distances, and goes to zero at r_{c2}.

The parameters of the potential were taken from Ref.,[7] where they have been favourably tested against DFT calculations. They are reported in Table S1.

Table S1: Parameters of the interaction potential. From Ref.[7]

	p	q	A (eV)	ξ (eV)	r_0 (Å)	$rc1$ (Å)	$rc2$ (Å)
Au-Au	10.139	4.033	0.2096	1.8153	2.88400	4.07859	4.99523
Pd-Pd	11.000	3.794	0.1715	1.7019	2.75064	3.88999	4.76425
Au-Pd	10.569	3.913	0.2764	2.0820	2.82732	4.07859	4.76425

Global optimization simulations are made by the Basin Hopping algorithm, using our own code.[8] For each size we initially consider ten different compositions from pure Pd to pure Au, increasing the Au content in the nanoparticle by steps of 10%. For each composition we perform at least three full global searches, in which geometric structure and chemical ordering are optimized simultaneously by combining brownian and exchange moves.[9] By comparing the results obtained at the different compositions we identify, for each size, the best structures of the three considered geometric motifs (Ih, Dh and TO). These structures are then employed in a new set of global optimization searches at fixed geometry, in which only the chemical ordering is optimized. In this set we increase the number of intermediate compositions in order to better analyse the region where the Ih motif is energetically favourable. All the simulations are 10^6 steps long.

Free energies are calculated starting from the best structures obtained in the global optimization. First, a local minimization is carried out at high precision, so that each atom's position is well established. The vibrational frequencies are then calculated via diagonalization of the mass weighted Hessian matrix associated with the SMATB potential used for global optimizations. Second derivatives are numerically estimated with the four point formula for finite differences, whereas diagonalization is achieved using LAPACK libraries.[10] The geometric average of the principal inertia moments, $\overline{I}_s$, is $(I_s^{xx} I_s^{yy} I_s^{zz})^{1/3}$. Finally h_s, the order of the symmetry group, is evaluated using SYMMOL.[11]

Experimental data on the distribution of the different structural motifs

In Figure S2 we present the evolution of the percentage of FCC truncated octahedra (TO), icosahedra (Ih), and decahedra (Dh) (shown in the y axis) in function of the length of the aggregation zone (x axis). By increasing L_{AZ} from 45 and 125 mm, and then decreasing ΔP at L_{AZ}=125 mm, one gradually increases the dwell time in the aggregation zone, so that the growth becomes closer and closer to thermodynamic equilibrium conditions, because the growing nanoparticles have more time to rearrange towards equilibrium structures during their growth.[12]

Each image refers to a different composition of the AuPd distributions. We note that in all the compositions the amount of Dh is by far lower than the other shapes, with very few exceptions. In the pure Pd for fast growing conditions, the amount of Dh is slightly lower than the one of TO. In $Au_{15}Pd_{85}$ at L_{AZ}=70 mm, %Dh is equal to %Ih, within the error range. In $Au_{25}Pd_{75}$ %Dh is always lower than 10%, making this motif almost negligible. Finally, in $Au_{35}Pd_{65}$ %Dh is lower than the other two motifs at all growing conditions, but the discrepancy of the three structures is not as remarkable as in the previous three distributions.

Global Optimization results

In Figure S3 we show the best TO, Ih and Dh for each of the four considered sizes (N = 150, 200, 250 and 300), as obtained in the first set of our global optimization searches (see the simulation methods above). We note that at size N = 150 and 300 Ih structures are very close to the perfect Ih of 147 and 309 atoms, respectively. At size N = 200 and 250, Ih structures are intermediate between the two perfect Ih clusters, with the presence of an incomplete outer shell. As discussed in the main text, the effect of Ih stabilization by Au

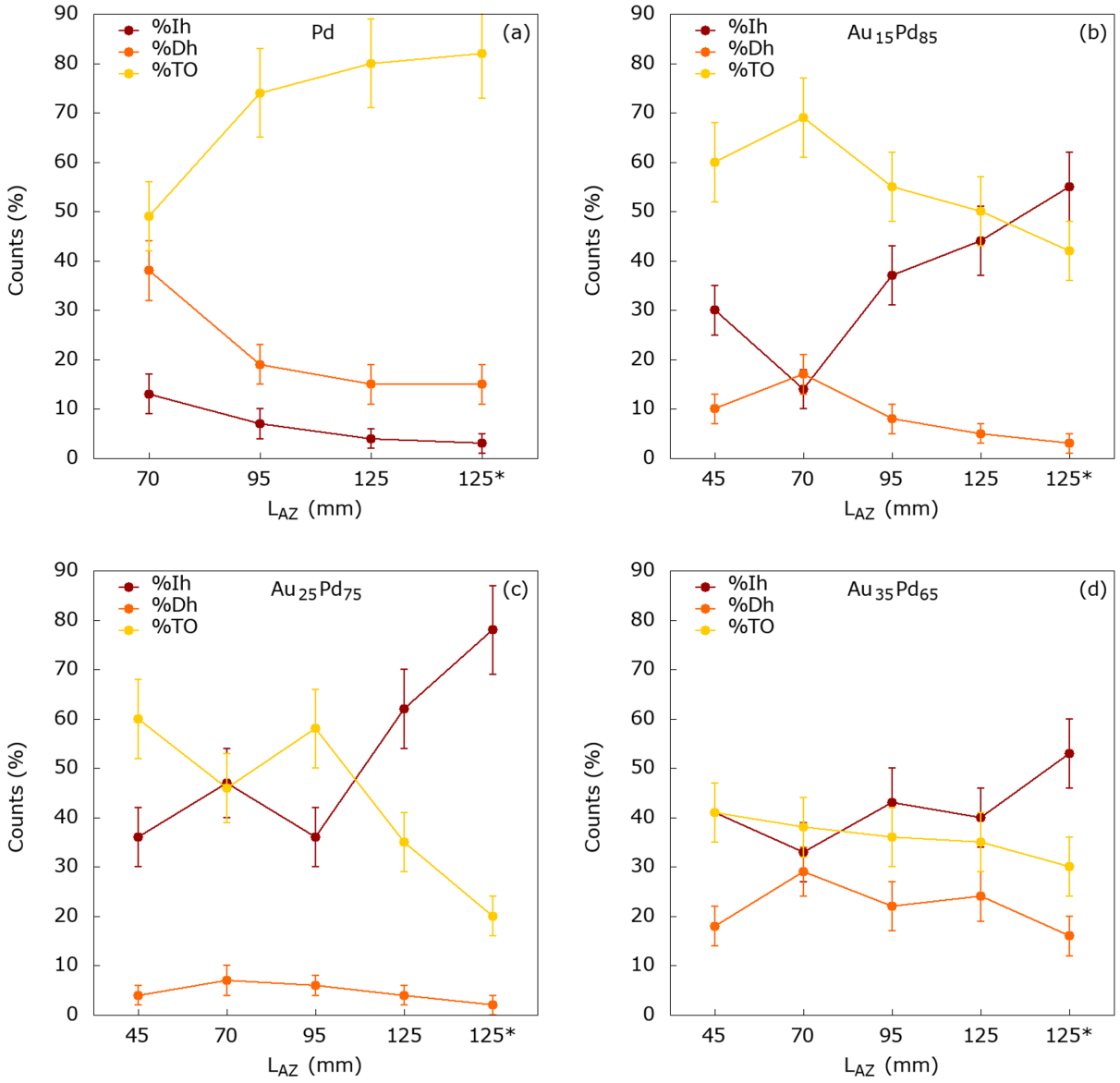

Figure S2: Evolution of the percentage of AuPd icosahedral (%Ih), decahedral (%Dh) and FCC truncated octahedral (%TO) on the total of structures analysed. The shape percentages are plot as a function of L_{AZ}. P_{DC}= 6x10^{-4} mbar for the first four L_{AZ} values and 7x10^{-3} mbar for the last point marked as "125* mm". Each image refers to a different composition as indicated in the image itself. Each curve refers to a different motif, as indicated in the legends. Error bars correspond to the square root of the number of counts.

surface atoms is more evident for the almost perfect Ih of size $N = 150$ and 300, but still present for the incomplete Ih structures of size $N = 200$ and 250.

In Figure S4 we show the results of the optimization of chemical ordering in the case of

$Au_{50}Pd_{250}$. This composition corresponds to the lowest value of ΔF for $N = 300$ (see Figure 3d in the main text), but it is indeed representative of all the Pd-rich compositions analysed. In each of the three geometric structures all Au atoms are placed on the nanoparticle surface, which presents an intermixed arrangement.

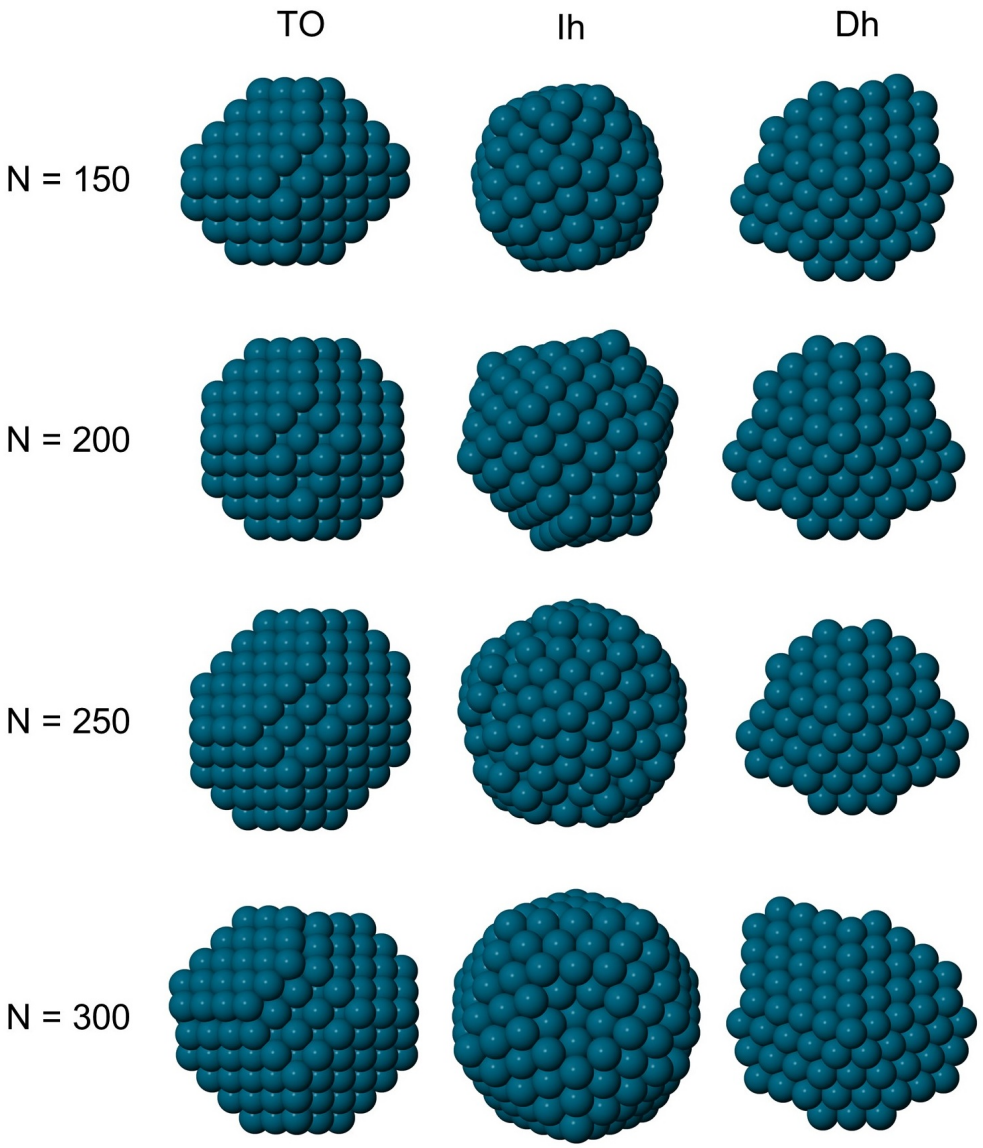

Figure S3: Best TO, Ih and Dh for $N = 150$, 200, 250 and 300 obtained in the global optimization searches. Here we show pure Pd clusters.

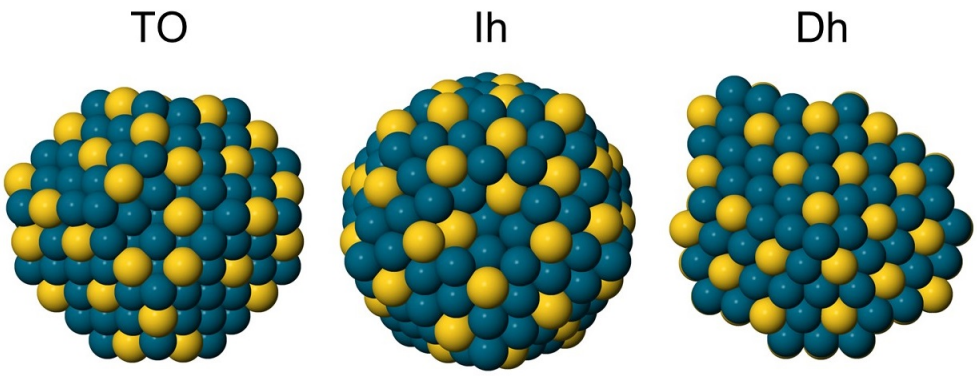

Figure S4: Best chemical ordering for $Au_{50}Pd_{250}$. Au and Pd atoms are colored in yellow and blue, respectively.

Free energy differences between Ih and Dh

In Figure S5 we report the free energy difference $\Delta F = F_{Ih} - F_{Dh}$ between the best Ih and the best Dh structure for different sizes and Pt-rich compositions. We consider the same sizes, compositions and temperatures at which the free energy difference $F_{Ih} - F_{TO}$ is evaluated (see Figure 3 in the main text). By comparing the two figures, we notice that the two free energy differences exhibit the same behaviour, taking minimum values in the same composition range. This result further confirms the existence of an interval of Pt-rich compositions in which Ih structures are stabilized, becoming competitive or even more favourable with respect to the other two geometric motifs.

Global optimization for size 561

In order to understand whether the effect of Ih stabilization by Au atoms is still present in larger nanoparticles, we calculate the energy difference ΔE between the perfect Ih of 561 atoms and the best TO structure of the same size, for different Pt-rich compositions. Results are shown in Figure S6. For pure Pd nanoparticles ΔE is positive, but it decreases while increasing the Au content and it takes negative values for a wide composition range. We therefore observe the same inversion of the relative stability of Ih and TO already discussed

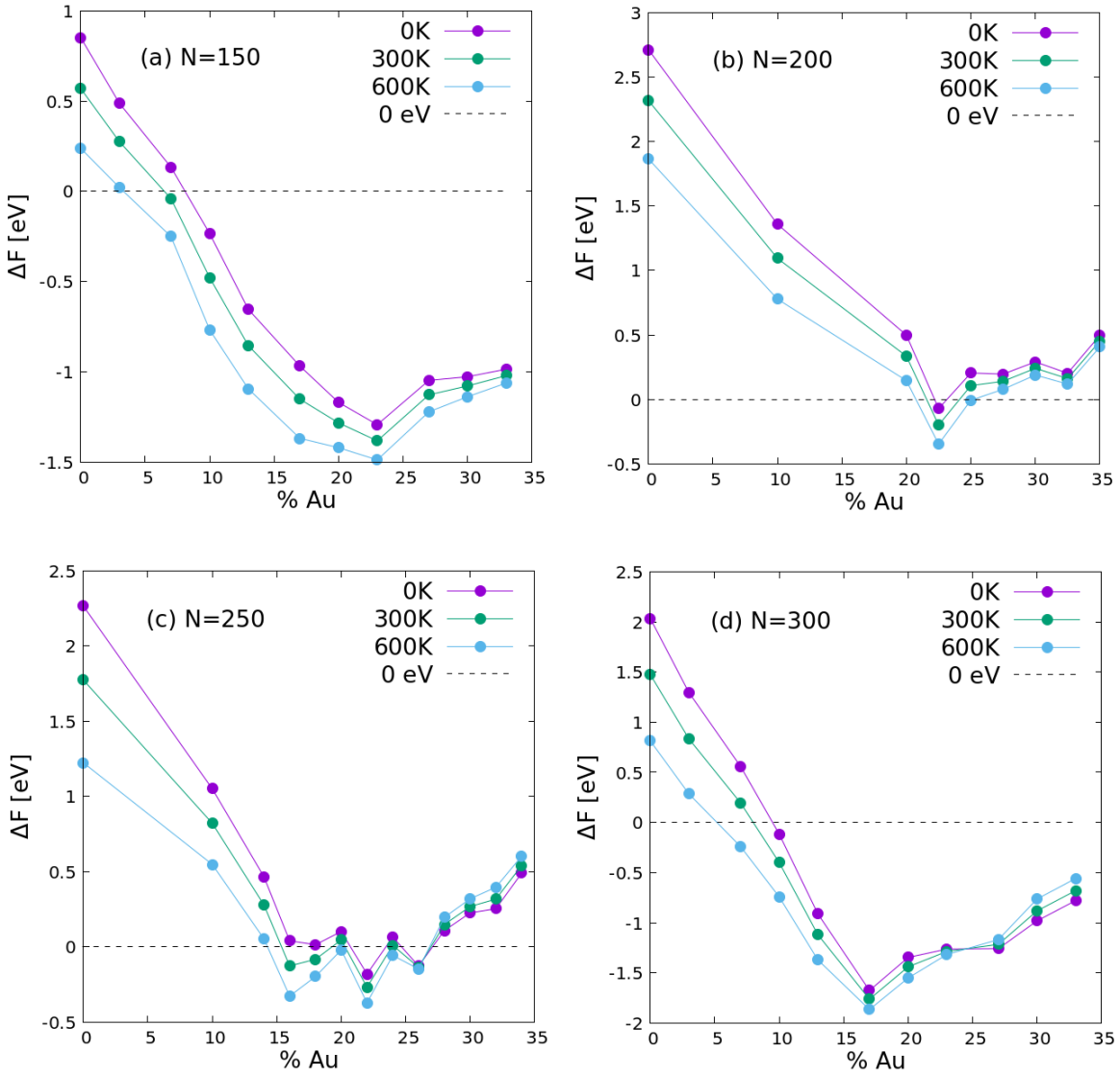

Figure S5: Free energy differences $\Delta F = F_{Ih} - F_{Dh}$ between the best Ih and Dh structures for different sizes and Pd-rich compositions. For $\Delta F < 0$ the Ih is favored over the Dh at the thermodynamic equilibrium, while for $\Delta F < 0$ the opposite holds.

for nanoparticles of smaller sizes.

We point out that, in this case, we do not calculate the free energy difference between the two structures but the difference between the energies obtained from our chemical ordering optimization searches. Anyway, we expect the entropic contribution to further stabilize Ih structures at higher temperatures, as already seen at smaller sizes.

Finally, we note that even in this case all Au atoms are placed in the surface of the

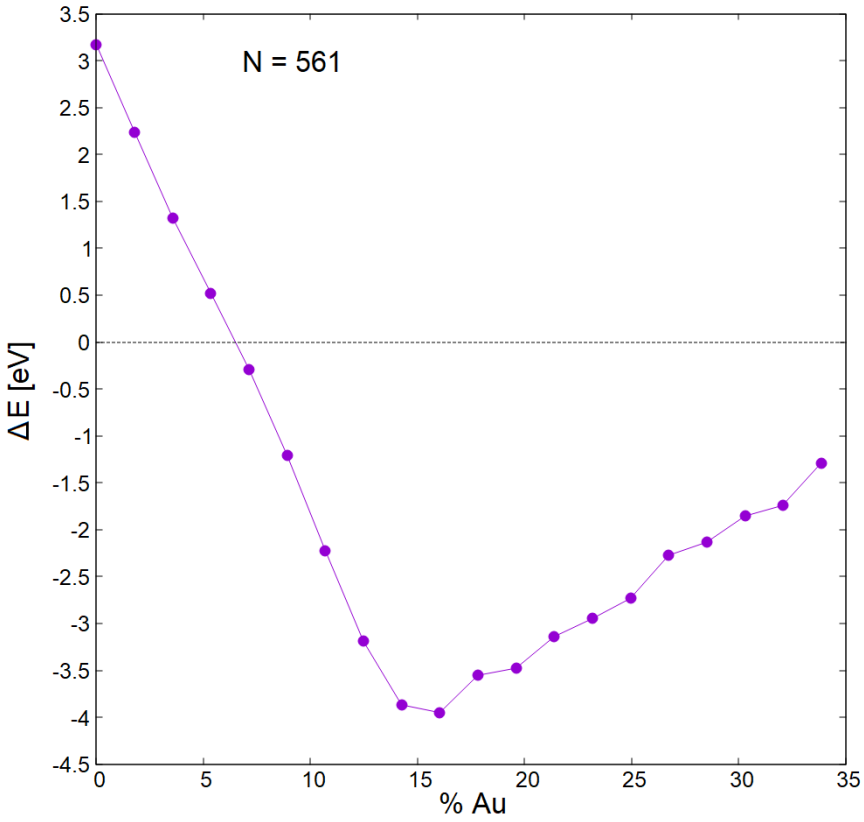

Figure S6: Energy difference ΔE between the best Ih and TO structures for different Pd-rich compositions at size 561 atoms.

optimized nanoparticles for all the considered compositions and for both geometric shapes, therefore we can state that the TO→Ih transition is due to the same mechanism of surface stress relaxation described in the main text.

References

(1) Johnson, G. E.; Colby, R.; Laskin, J. Soft landing of bare nanoparticles with controlled size, composition, and morphology. *Nanoscale* **2015**, *7*, 3491–3503.

(2) Mayoral, A.; Mejia-Rosales, S.; Mariscal, M. M.; Perez-Tijerina, E.; Jose-Yacaman, M. The Co-Au interface in bimetallic nanoparticles: a high resolution STEM study. *Nanoscale* **2010**, *2*, 2647–2651.

(3) Nelli, D.; Cerbelaud, M.; Ferrando, R.; Minnai, C. Tuning the coalescence degree in the growth of Pt–Pd nanoalloys. *Nanoscale Adv.* **2021**, *3*, 836–846.

(4) Gupta, R. P. Lattice relaxation at a metal surface. *Phys. Rev. B* **1981**, *23*, 6265.

(5) Rosato, V.; Guillopé, M.; Legrand, B. Thermodynamical and structural properties of f.c.c. transition metals using a simple tight-binding model. *Phil. Mag. A* **1989**, *59*, 321.

(6) Cyrot-Lackmann, F.; Ducastelle, F. Binding Energies of Transition-Metal Atoms Adsorbed on a Transition Metal. *Phys. Rev. B* **1971**, *4*, 2406–2412.

(7) Pittaway, F.; Paz-Borbon, L. O.; Johnston, R. L.; Arslan, H.; Ferrando, R.; Mottet, C.; Barcaro, G.; Fortunelli, A. Theoretical Studies of Palladium-Gold Nanoclusters: Pd-Au Clusters with up to 50 Atoms. *The Journal of Physical Chemistry C* **2009**, *113*, 9141–9152.

(8) Rossi, G.; Ferrando, R. Searching for low-energy structures of nanoparticles: a comparison of different methods and algorithms. *J. Phys. Cond. Mat.* **2009**, *21*, 084208.

(9) Ferrando, R. *Structure and Properties of Nanoalloys*; Frontiers of Nanoscience, Volume 10; Elsevier, 2016.

(10) Anderson, E.; Bai, Z.; Bischof, C.; Blackford, S.; Demmel, J.; Dongarra, J.; Du Croz, J.; Greenbaum, A.; Hammarling, S.; McKenney, A. et al. *LAPACK Users' Guide*, 3rd ed.; Society for Industrial and Applied Mathematics: Philadelphia, PA, 1999.

(11) Pilati, T.; Forni, A. SYMMOL: a program to find the maximum symmetry group in an atom cluster, given a prefixed tolerance. *Journal of Applied Crystallography* **1998**, *31*, 503–504.

(12) Plant, S. R.; Cao, L.; Palmer, R. E. Atomic structure control of size-selected gold nanoclusters during formation. *Journal of the American Chemical Society* **2014**, *136*, 7559–7562.